photonics

MDPI

Article

Wide-Temperature-Range Stability of a Compact LNOI Hybrid Plasmonic TE-Pass Polarizer for Fiber-Optic Gyroscope Applications

Hanyi Zhang [1,†], Rong Fan [1,†], Yinzhou Zhi [2], Lulu Fang [1], Wenxuan Cheng [1], Yujie Wang [1], Jianfeng Bao [3,*] and Lijing Li [1,*]

[1] School of Instrumentation and Optoelectronic Engineering, Beihang University, Beijing 100191, China; by2117118@buaa.edu.cn (H.Z.); fanrong_buaa@outlook.com (R.F.); zb2517003@buaa.edu.cn (L.F.); cwx2025@buaa.edu.cn (W.C.); wyj13831391657@163.com (Y.W.)
[2] Beijing Institute of Control Engineering, Beijing 100094, China; zy18df104@buaa.edu.cn
[3] School of Physics and Electronic Information Engineering, Ningxia Normal University, Guyuan 756099, China
* Correspondence: jianfengbao142857@126.com (J.B.); lilijing@buaa.edu.cn (L.L.)
† These authors contributed equally to this work.

Abstract

In this study, we present a thermal-aware design of a compact hybrid plasmonic grating (HPG) TE-pass polarizer on X-cut lithium niobate on insulator (LNOI) for fiber-optic gyroscopes (FOGs). In a three-dimensional simulation, the optimization of the trapezoidal sidewall angle (θ = 78°) and the thickness of the Ag grating (13 nm) yield a polarization extinction ratio of 36.2 dB at 1550 nm (with a peak of 41.4 dB at 1548 nm) within a sub-10 µm grating length. This represents a ~3–8 dB improvement over prior LNOI HPG polarizers at the same footprint. A multiphysics thermo-optic analysis over the wide industrial FOG envelope (from −45 to +85 °C) demonstrates that the operating-wavelength polarization extinction ratio remains within the range of 24.7–36.2 dB across the entire 130 K span (worst case 24.7 dB at −25 °C), constrained solely by a modest 10 pm/K Bragg detuning stemming from the pronounced (~5) thermo-optic anisotropy of LN. The insertion loss exhibits a negligible drift of merely 0.73 dB. A fabrication tolerance study identified the Ag thickness as the predominant budgetary constraint (±1 nm tolerance, PER dropping ~10 dB at the resonance edge), while the ridge width and oxide buffer demonstrated comparatively greater flexibility. The device, therefore, fulfills the criteria for FOG-grade polarization suppression across most of the operational temperature range. The −25 °C point is established at the 25 dB threshold, thereby providing concrete design guidelines for ensuring environmentally stable on-chip polarization control on LNOI.

Keywords: lithium niobate on insulator (LNOI); hybrid plasmonic grating; TE-pass polarizer; polarization extinction ratio (PER); thermo-optic effect; temperature stability; fiber-optic gyroscope; integrated photonics

Check for updates

Received: 1 June 2026
Revised: 12 June 2026
Accepted: 13 June 2026
Published: 15 June 2026

1. Introduction

Fiber-optic gyroscopes (FOGs) are a cornerstone of modern inertial navigation, valued for their solid-state construction, wide dynamic range, and long-term reliability in aerospace, defense, and autonomous-platform applications [1,2]. The accuracy of an FOG is fundamentally limited by polarization non-reciprocity. Any residual cross-polarized light that enters the Sagnac interferometer produces a polarization-related bias error. This

https://doi.org/10.3390/photonics13060585

error directly degrades the gyroscope's bias stability and scale-factor accuracy [3]. A high-extinction-ratio polarizer that is integrated into the optical path is, therefore, an indispensable component. This component is necessary to suppress the unwanted polarization state in order to preserve reciprocity. Furthermore, navigation- and tactical-grade FOGs must operate over a wide industrial temperature range, typically from −45 °C to +85 °C. Over this range, the polarizer must maintain its extinction performance without the need for active control. The amalgamation of these requirements—namely, high polarization extinction, compact integration, and wide-temperature stability—has prompted the development of an integrated polarizer that has been specifically engineered for thermal robustness.

Lithium niobate on insulator (LNOI) has emerged as a leading platform for integrated photonics, owing to its strong electro-optic coefficient, broad transparency window from visible to mid-infrared, and compatibility with CMOS fabrication processes. Recent demonstrations of high-speed Mach–Zehnder modulators [4,5], among other functional photonic devices [6], have established LNOI as a pivotal component for next-generation optical communication and sensing systems. However, the strong birefringence of lithium niobate, in conjunction with the multimode nature of typical LNOI ridge waveguides, renders polarization management a critical design consideration. An effective on-chip polarizer is imperative for the suppression of undesired polarization modes and the maintenance of system performance, particularly in interferometric applications such as fiber-optic gyroscopes (FOG), where polarization extinction exerts a direct influence on bias stability [7,8].

A plethora of polarizer architectures have been proposed on LNOI, including shallow-etched ridge waveguides based on mode leakage [9], subwavelength gratings [7], Euler-bend waveguides [10], and hybrid plasmonic structures [11–14]. Among the aforementioned approaches, the hybrid plasmonic grating (HPG) approach offers a unique balance between compactness and performance. The integration of a thin metallic grating above a thin SiO_2 spacer on the LN ridge waveguide enables the simultaneous exploitation of surface plasmon polariton coupling, Bragg reflection, and mode mismatch. This integration allows for the selective suppression of the TM mode while transmitting TE with minimal loss [12,15]. Dai et al. demonstrated a 9 µm long HPG TE-pass polarizer on X-cut LNOI, achieving a polarization extinction ratio (PER) over 20 dB across a wavelength range of (1470, 1700) nm, with a peak PER of 33 dB and insertion loss (IL) below 2.3 dB in the C-band [13]. The compact footprint of HPG differentiates it from competing schemes, including shallow-etched waveguides (operating on the millimeter scale [9]) and recent Euler-bend designs (>180 µm [10]).

Notwithstanding its auspicious performance, the practical implementation of HPG polarizers on LNOI poses numerous challenges that have not been systematically addressed in the extant literature. First, the strong mode coupling at sub-wavelength feature sizes (Ag thickness ≈ 15 nm, SiO_2 spacer ≈ 40 nm) demands careful finite-element method (FEM) modeling. In this context, mesh convergence, port mode selection, and symmetry boundary condition handling can significantly influence the simulated performance. However, these methodological aspects are seldom reported in detail. Secondly, while single-parameter fabrication tolerance has been the subject of investigation [14], the joint sensitivity to coupled multi-parameter deviations—such as simultaneous variation in ridge width and sidewall inclination—remains underexplored, although it is critical for practical fabrication. Thirdly, a comprehensive design framework integrating rigorous simulation methodology with practical fabrication considerations is lacking. Most critically, fiber-optic gyroscopes must operate reliably across a wide temperature range (from −45 to +85 °C). However, existing LNOI polarizer designs have been characterized only at room temperature. Due to the pronounced anisotropy of the thermo-optic response of LN, characterized by a ratio of $\mathrm{d}n_\mathrm{e}/\mathrm{dT}$ to $\mathrm{d}n_\mathrm{o}/\mathrm{dT}$ of approximately five at 1.55 µm, the Bragg resonance undergoes a detuning in response to temperature fluctuations, resulting in a degradation of the in-band polarization extinction ratio. This engineering gap remains unaddressed in a systematic manner.

In this study, we present research on a compact HPG TE-pass polarizer on X-cut LNOI, with a focus on thermal-aware design and optimization. The contributions of this study are multifaceted and can be enumerated as follows:

First, we present a novel thermo-optic multiphysics analysis for LNOI HPG polarizers. This analysis quantifies the Bragg detuning rate, which is determined by the sum of the two modal thermo-optic coefficients, as well as the resulting polarization-extinction-ratio behavior across the FOG operating temperature range. This analysis represents a significant advancement in the field of optical polarizers.

The establishment of a rigorous FEM simulation methodology is imperative for the explicit treatment of mesh convergence, port-mode selection criteria, and symmetric boundary conditions for the TE and TM polarizations.

The geometric parameters are systematically optimized, including the width of the ridge (w_{top}), the inclination of the side walls (θ), the thickness of the Ag (h_{m}), the thickness of the SiO_2 spacer (h_{o}), the period of the grating ($\mathit{\Lambda}$), and the period number (N).

We then analyzed the joint fabrication tolerance under coupled parameter variations. The optimized device was benchmarked against representative competing on-chip polarizer platforms. These platforms included the prior LNOI HPG, shallow-etched ridge, subwavelength-grating, and Euler-bend designs. This comparison highlighted the combined advantage of the device in compactness, polarization extinction ratio, and wide-temperature stability for FOG integration. The optimized sub-10 μm device achieves a polarization extinction ratio of 36.2 dB at 1550 nm (peak 41.4 dB at 1548 nm) with insertion loss ~3.5 dB, and maintains a PER within 24.7–36.2 dB across the full −45 to +85 °C range.

2. Device Structure and Basic Theory

The device is a hybrid plasmonic grating (HPG) integrated on X-cut, Y-propagating lithium niobate on insulator (LNOI). Figure 1 illustrates the three-dimensional geometry. The formation of an X-cut, Y-propagating LN ridge waveguide, characterized by a top width of w_{top} = 1 μm, a trapezoidal cross-section angle of θ, and a total film thickness of 600 nm with etched depth 300 nm, is achieved on a 3 μm SiO_2 buried oxide layer. A 40 nm thick silicon dioxide buffer layer h_{o} is deposited over the ridge crest. Above this layer, a periodic silver grating is patterned with a period of 1.64 μm and N = 6 periods. This results in a total grating length of 9.84 μm, which is approximately 12 μm including input and output transitions. Each unit cell consists of a wide metal tooth with a width of w_1 = 0.86 μm and a narrow gap with a width of w_2 = 0.1 μm. The thickness of the Ag layer, h_{m}, is the primary optimization variable (see Section 4).

The complete set of material and geometric parameters used throughout the simulations is summarized in Table 1. The lithium niobate refractive indices and their thermo-optic coefficients are taken from [16,17], capturing the strong birefringence and the anisotropic thermo-optic response ($\mathrm{d}n_{\mathrm{e}}/\mathrm{dT} \approx 5 \times \mathrm{d}n_{\mathrm{o}}/\mathrm{dT}$) that underlies the device's thermal behavior; the silver permittivity follows the Johnson–Christy data and is treated as temperature invariant.

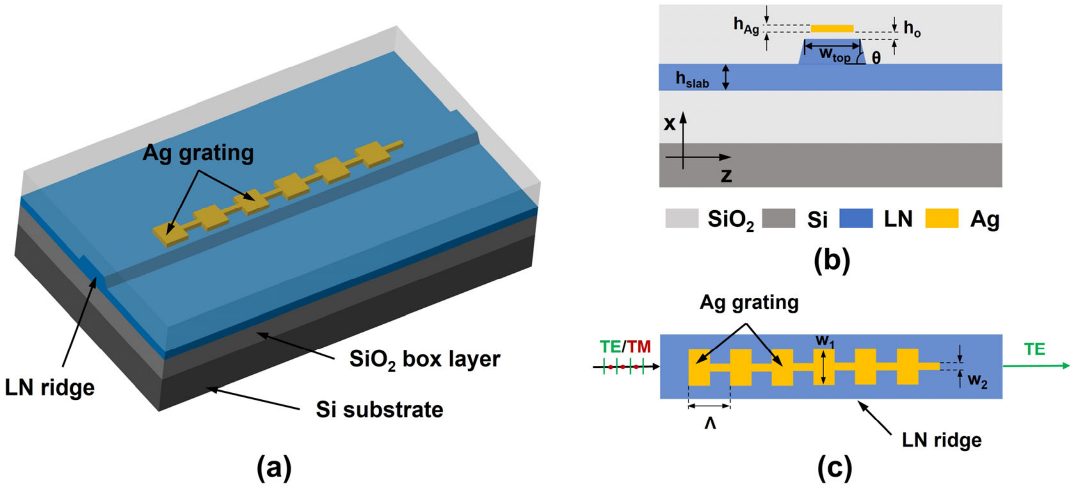

Figure 1. Schematic of the proposed hybrid plasmonic grating (HPG) TE-pass polarizer on X-cut LNOI. (**a**) Three-dimensional device geometry; (**b**) cross section of the HPG region (baseline ridge top width w_{top} = 1 µm, with slab LN layer thickness h_{slab} = 300 nm, sidewall angle θ, SiO_2 buffer h_o = 40 nm, Ag thickness h_m); (**c**) cross section along with the propagation direction (period Λ = 1.64 µm, N = 6).

Table 1. Material and structural parameters used in the simulations (λ = 1550 nm, T = 25 °C unless noted).

Parameter	Symbol	Value	Source/Note
LN extraordinary index	n_e	2.14	Zelmon et al.
LN ordinary index	n_o	2.21	Zelmon et al.
LN TO coeff. (e-axis)	$\mathrm{d}n_e/\mathrm{dT}$	3.3×10^{-5} K^{-1}	Moretti et al.
LN TO coeff. (o-axis)	$\mathrm{d}n_o/\mathrm{dT}$	6×10^{-6} K^{-1}	Moretti et al.
SiO_2 index	n_{SiO2}	1.444	—
Ag permittivity	$\varepsilon_{\mathrm{Ag}}$	Johnson–Christy	T-invariant
Ridge top width	w_{top}	1000 nm	optimized
LN slab thickness	h_{slab}	300 nm	fixed
Sidewall angle	θ	78°	optimized
Ag thickness	h_m	13 nm	optimized
SiO_2 buffer	h_o	40 nm	optimized
Grating period	Λ	1.64 µm	q = 4 Bragg
Period number	N	6	—
Operating wavelength	λ	1550 nm	C-band

The polarization-selective mechanism exploits three cooperating effects. First, surface-plasmon polariton (SPP) coupling [18] at the Ag/SiO_2 interface attenuates the TM_0 mode, whose dominant E_y component couples resonantly to the SPP field. The TE_0 mode, with dominant E_x component oriented parallel to the crystal c-axis, does not fulfill the SPP phase-matching condition and propagates with low excess loss. Second, Bragg back reflection of the TM_0 mode is established when the grating period satisfies the following:

$$\Lambda = q\lambda/(n_{\mathrm{eff,TE}} + n_{\mathrm{eff,TM}}) \tag{1}$$

where q is the diffraction order. Third, mode-mismatch loss at each metal tooth further penalizes TM transmission [14]. The combined effect yields a high polarization extinction ratio (PER) for TE transmission with insertion loss (IL) well below the plasmonic contribution alone.

Since LN is an anisotropic negative uniaxial crystal ($n_e < n_o$ at λ = 1550 nm) and the crystal c-axis lies along the COMSOL (version 6.3 AB, Stockholm, Sweden) x-direction (horizontal, in-plane) for the X-cut orientation, the dielectric tensor is diagonal: $\varepsilon_{xx} = n_e^2$, $\varepsilon_{yy} = n_o^2$, $\varepsilon_{zz} = n_o^2$. The TE_0 mode, therefore, samples predominantly n_e, and TM_0 samples n_o. This anisotropy has direct consequences for thermal behavior, as discussed in Section 5.

3. Simulation Methods

3.1. Three-Dimensional Finite-Element Model

Full three-dimensional electromagnetic simulations were performed with the Frequency Domain module of COMSOL Multiphysics. The computational domain encompasses the complete ~9.84 µm grating length plus transitions, including input and output waveguide tapers, and is terminated by perfectly matched layer (PML) absorbers on all lateral and longitudinal boundaries. The PML thickness is set to 1 µm and the PML scaling factor optimized to achieve back reflection below −60 dB across the 1450–1700 nm range.

The simulation domain was discretized with an adaptive tetrahedral mesh, shown in Figure 2. The mesh is strongly refined in the Ag grating and the thin SiO_2 buffer, where the surface-plasmon field exhibits the steepest gradients, and is progressively coarsened toward the perfectly matched layer (PML) boundaries to limit the total element count. Mesh convergence was confirmed by successively refining the metal-region elements until the computed PER varied by less than 0.3 dB.

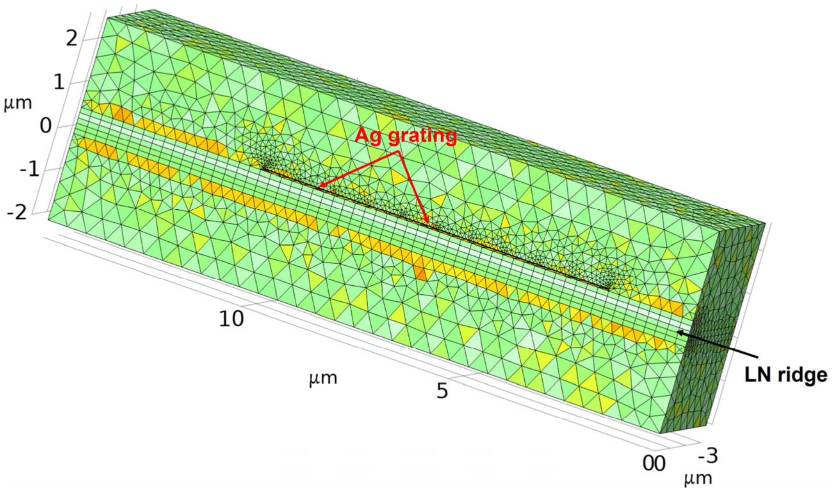

Figure 2. Three-dimensional finite element mesh of the HPG region, refined around the Ag grating and SiO_2 buffer where the plasmonic field varies most steeply, and coarsened toward the domain boundaries.

Mesh convergence was validated against a sequence of four refinement levels. The final mesh uses a maximum element size of $\lambda/(20{\cdot}n_{\text{eff}})$ in the LN core and is further refined to $h_m/5$ inside the Ag layer to resolve the skin-depth scale field variation. The total degree-of-freedom count at 1550 nm is approximately 4×10^6. A convergence criterion of less than 0.3 dB change in PER between successive refinement levels was adopted.

Ports are defined on the input and output waveguide cross sections with boundary-mode analysis (BMA) to extract the fundamental TE_0 and TM_0 eigenmodes. The TE and TM responses are computed in independent studies using symmetric and anti-symmetric boundary conditions, respectively, on the vertical symmetry plane, which halves the computational domain without loss of generality for the modes of interest. Transmission is quantified via the built-in port transmittance, which normalizes output power to the portinjected modal power, and is thus insensitive to the choice of cross-sectional integration boundary. The polarization extinction ratio is defined as:

$$\mathrm{PER} = -10log_{10}(P_{\mathrm{TM}}/P_{\mathrm{TE}}) \tag{2}$$

The insertion loss for the TE pass band is $\mathrm{I}L = -10log_{10}(P_{\mathrm{TE}}/P)$.

3.2. Two-Dimensional Mode Analysis

Complementary two-dimensional cross-sectional mode analysis (FEM eigenvalue solver) was performed on a separate model to track n_{eff} for TE_0, TM_0, and hybrid plasmonic modes across wavelength and temperature. This model is computationally inexpensive and was used to derive the Bragg detuning rate $\delta\lambda_{\mathrm{B}}/\delta T$ analytically from the extracted mode indices before running the full 3D temperature sweeps. Mode identity was assigned at each wavelength and temperature by simultaneously evaluating the LN-core confinement factor Γ_{EO}, the TE polarization purity, and the overlap integral with the T_0 reference eigenmode, following the branch-tracking protocol. This protocol prevents spurious branch jumping at the anti-crossing between the hybrid plasmonic mode and the dielectric TM_0 branch.

Figure 3 contrasts the TE and TM behavior that underlies the polarizer's operation. In the cross-sectional profiles, the TE_0 mode remains well confined within the LN ridge (a), whereas the hybrid TM mode is pulled toward the Ag layer and strongly absorbed (c). The three-dimensional propagation views confirm this selectivity: the TE mode traverses the grating with little attenuation (b), while the TM mode decays within the first few periods (d), establishing the TE-pass, TM-block function.

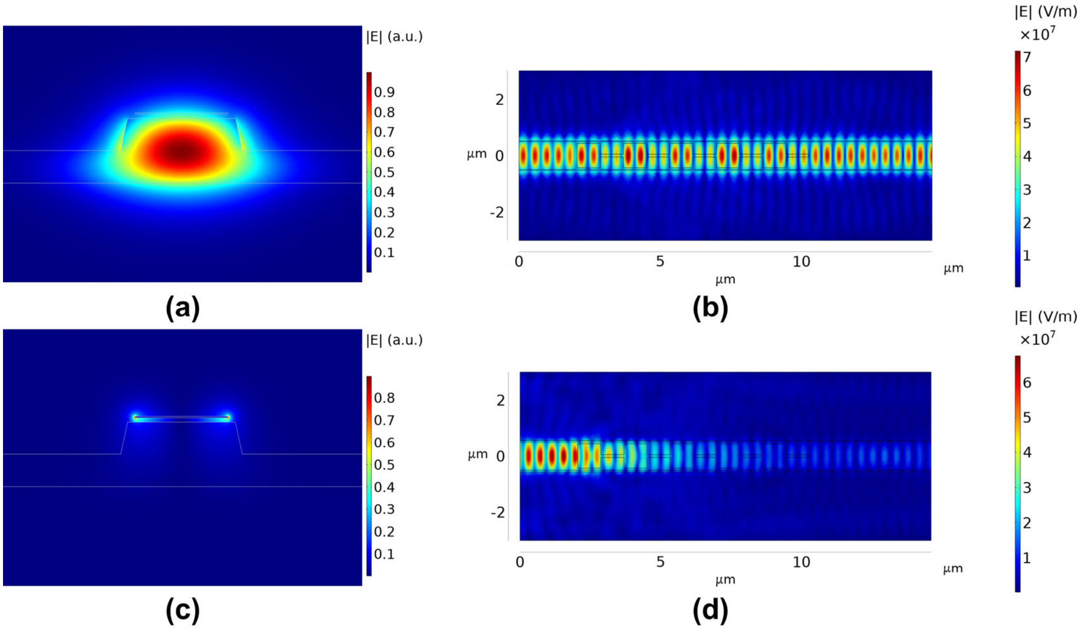

Figure 3. Electric field distributions of the HPG polarizer at θ = 78°, $\mathrm{h_m}$ = 13 nm, λ = 1550 nm, T = 25 °C. (**a**,**c**) Two-dimensional cross-sectional mode profiles $|E|$ (normalized) of (**a**) the TE_0 mode and (**c**) the hybrid TM mode; (**b**,**d**) three-dimensional propagation profiles along Y direction for (**b**) TE and (**d**) TM input.

3.3. Multiphysics Framework: Thermo-Optic Channel

LN supports four index-perturbation channels under coupled thermo-electro-mechanical loading: the Pockels effect, the piezo/photoelastic effect, the thermo-optic (TO) effect, and pyroelectric polarization [19]. For the passive electrically floating HPG polarizer studied here, the first two channels carry no driving field (no biased electrode) and contribute zero net index perturbation. Pyroelectric charge accumulating on the LN/SiO_2 interface is screened by surface conductivity on operational timescales; its residual contribution to Δn_{eff} is of order 10^{-7}, three to four decades below the direct TO term. Lattice expansion across the 130 K FOG temperature excursion (-45 to +85 °C) reaches $\varepsilon \sim 2 \times 10^{-3}$, giving a photoelastic $\Delta n_{\mathrm{LN}} < 10^{-6}$ and a geometric distortion at the nanometer scale.

The multiphysics analysis is therefore reduced to the thermo-optic channel alone. Temperature enters the simulation as a uniform scalar parameter T (no heat-transfer solver is required, because the device lacks internal heat sources). The LN refractive-index tensor is written as:

$$n_{LN}(\lambda, \mathrm{T}) = \begin{pmatrix} n_e(\lambda) + (\mathrm{d}n_e/\mathrm{dT}) \triangle T & 0 & 0 \\ 0 & n_o(\lambda) + (\mathrm{d}n_o/\mathrm{dT}) \triangle T & 0 \\ 0 & 0 & n_o(\lambda) + (\mathrm{d}n_o/\mathrm{dT}) \triangle T \end{pmatrix} \quad (3)$$

$\triangle T = T - T_0$, with room-temperature Sellmeier values $n_e(\lambda)$ and $n_o(\lambda)$ taken from Zelmon et al. [16] and thermo-optic coefficients $\frac{\mathrm{d}n_o}{\mathrm{d}T} \approx 6 \times 10^{-6}\mathrm{K}^{-1}$ (ordinary axis) and $\frac{\mathrm{d}n_e}{\mathrm{d}T} \approx 3.3 \times 10^{-5}\mathrm{K}^{-1}$ (extraordinary axis) from Moretti et al. (2005) [17,20]. The strong (factor ~5×) anisotropy between the two TO coefficients in LN at 1.55 µm is physically significant for this device because for TE_0 samples predominantly n_e (large $\mathrm{d}n_e/\mathrm{d}T$) and TM_0 samples n_o (small $\mathrm{d}n_o/\mathrm{d}T$), the Bragg condition acquires a polarization-asymmetric temperature dependence. This asymmetry is precisely what enables ER to remain thermally robust at the operating wavelength—the TM_0 branch contributes only a weak detuning while the TE_0 pass band drifts more uniformly with temperature, preserving the contrast.

The Ag permittivity is taken from the Johnson–Christy dataset and held temperature invariant. Within the Drude framework, the electron–phonon scattering rate scales as $\gamma(T) \approx \gamma_0(1 + \alpha T)$ with $\alpha \approx 4 \times 10^{-3}\mathrm{K}^{-1}$, yielding a fractional change in $\mathrm{Im}(\varepsilon^{\mathrm{AG}})$ of an order 15% over the 130 K FOG span. At λ = 1550 nm, the resulting drift in the Ag extinction coefficient is below 0.15 (against a baseline $\kappa \approx 11.4$), bounding the IL drift to less than 0.2 dB across the FOG operating range—at least an order of magnitude smaller than the PER variation driven by Bragg detuning, and consistent with the simulated 0.73 dB total IL drift of which the Ag contribution is a fraction. Therefore, Ag dispersion is held fixed, with the residual noted in the discussion. The SiO_2 TO coefficient ($\frac{\mathrm{d}n}{\mathrm{d}T} \approx 1.0 \times 10^{-5}\mathrm{K}^{-1}$) is included in the material model for completeness; its contribution to Δn_{eff} is below 10^{-6}.

4. Geometry Optimization at Room Temperature

4.1. Bragg Condition and Parameter Space

The grating period obeys the Bragg back reflection condition $\Lambda = q\lambda/(n_{\mathrm{eff,TE}} + n_{\mathrm{eff,TM}})$, where q is the diffraction order. A two-dimensional eigenmode analysis at T = 25 °C and the nominal ridge width w_{top} = 1 µm gives $n_{\mathrm{eff,TE}} \approx 1.9033$ and $n_{\mathrm{eff,TM}} \approx 1.8932$ (sum 3.797), so that the chosen period Λ = 1.64 µm corresponds to the q = 4 order, $q\lambda/(n_{\mathrm{eff,TE}} + n_{\mathrm{eff,TM}})$ = 1.633 µm, within 0.4% of the design value. Although no > ne, the effective indices satisfy $n_{\mathrm{eff,TE}} > n_{\mathrm{eff,TM}}$ because the TE0 mode is tightly confined in the high-index LN core, whereas the TM0 field is partly drawn into the lower-index SiO_2/Ag region (a smaller LN confinement factor); the effective indices are thus set by the modal overlap with each material rather than by the bulk anisotropy alone. Relative to a first-order design, this higher-order grating relaxes the minimum feature size requirement while still providing strong TM back reflection at the required number of periods. The resulting narrow-band, high-Q resonance is consistent with the sharp PER peaks seen in the parameter sweeps of Sections 4.2 and 4.3. The diffraction order q (which fixes the period Λ) and the period number N (which fixes the cumulative reflection depth) are independent design quantities: here $q = 4$ sets $\Lambda = 1.64$ µm, while $N = 6$ period matching—give a total grating length of 9.84 µm and provide ample margin for complete TM extinction, since the propagation profiles in Section 4.4 show the TM mode decaying within the first two periods. The minor TE/TM index contrast ($\Delta n_{\text{eff}} \approx 0.010$), which is characteristic of the inclined-ridge X-cut LNOI waveguide, is precisely why a metallic grating—rather than pure dielectric birefringence—is required to achieve a high polarization extinction ratio. The primary free parameters for PER optimization are, therefore, the sidewall inclination angle θ, which sets the TE/TM modal-overlap contrast, and the Ag thickness $\mathrm{h_m}$, which sets the SPP coupling strength and the Bragg reflectivity.

4.2. Sidewall Angle Optimization

A coarse two-parameter scan was first carried out to localize the optimal region before committing to fine sweeps. Table 2 lists the PER at λ = 1550 nm for sidewall angles from 50° to 85° and Ag thicknesses of 5, 10, and 20 nm. The PER rises toward larger θ and peaks near $h_m = 10$ nm, identifying the $\theta \approx 80°$, $h_m \approx 10$ nm neighborhood as the starting point; the subsequent single-parameter sweeps (Sections 4.2 and 4.3) refine this to the final $\theta = 78°$, $h_m = 13$ nm optimum.

Table 2. Coarse PER (dB) map versus sidewall angle θ and Ag thickness h_m (λ = 1550 nm, T = 25 °C), used to locate the optimum ($\theta \approx 80°$, $h_m \approx 10$ nm) before the fine sweeps.

θ (Deg)	h_m = 5 nm	h_m = 10 nm	h_m = 20 nm
50	28.0	29.3	24.9
55	29.5	30.4	26.0
60	29.0	29.2	26.7
65	29.9	32.4	27.4
70	31.2	31.1	27.7
75	30.5	31.3	27.0
80	32.4	33.0	28.2
85	33.0	30.1	27.3

A wavelength-resolved sweep over $\theta \in \{74°, 76°, 78°, 80°, 82°\}$ at $\mathrm{h_m} = 13$ nm, λ = 1500–1600 nm, and T = 25 °C was performed to identify the optimal sidewall angle. Figure 4b plots PER(λ) for each θ. The Bragg peak appears at λ ≈ 1540–1548 nm and varies systematically with θ: the peak PER reaches 41.4 dB at $\theta = 78°$, compared with 35.6 dB (74°), 29.9 dB (76°), 32.0 dB (80°), and 31.1 dB (82°); at the 1550 nm operating wavelength, the optimized device ($\theta = 78°$) yields 36.2 dB (Section 4.4). The global PER maximum across the spectrum is 41.4 dB at $\theta = 78°$, λ = 1548 nm. Therefore, $\theta = 78°$ is selected as the room-temperature design baseline. The 6–11 dB PER margin at the optimum over the neighboring angles indicates a tolerance-to-sidewall etch variation that is well within standard ICP-RIE process control.

4.3. Fine Sweep of h_m at $\theta = 78°$

A refined sweep over $h_m \in [8, 16]$ nm in 0.5 nm steps at θ = 78°, λ = 1550 nm, and $T = 25$ °C was performed to localize the optimal Ag thickness. The PER exhibits a sharp resonance peak of 36.2 dB at $h_m = 13$ nm, dropping to ≈ 28 dB at ±1 nm. The practical fabrication window is defined by this shoulder: PER > 25 dB is maintained over $h_m \in [11.5, 14]$ nm. Beyond this window, the PER falls monotonically on both sides, reaching ≈ 16 dB at $h_m = 8$ nm (under-coupled SPP regime) and ≈ 34 dB at $h_m = 16$ nm (over-damped regime where metallic absorption dominates), consistent with the Ag skin-depth argument of Section 4.2. The narrow window giving peak PER is achievable with precision electron-beam evaporation or atomic-layer deposition of Ag and can be monitored in situ by reflectometry during deposition. The room-temperature design baseline is thus fixed at θ = 78° and h_m = 13 nm. Notably, the independent θ, w_{top}, and h_m sweeps all return consistent PER at the nominal point, confirming that this geometry is a genuine joint optimum rather than a single-parameter artefact.

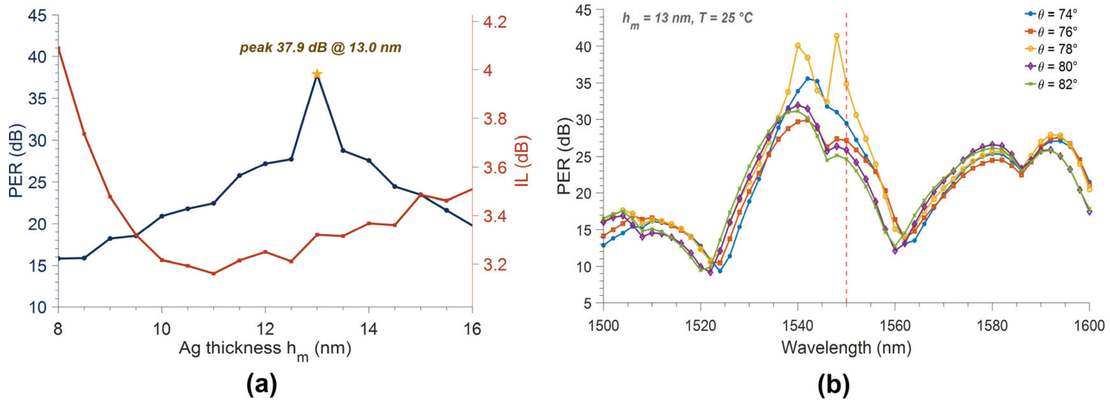

Figure 4. Room-temperature geometry optimization at T = 25 °C. (**a**) PER and IL versus Ag thickness h_m at θ = 78°, λ = 1550 nm (PER, left axis; IL, right axis), with the peak at h_m = 13 nm; (**b**) PER(λ) for sidewall angles $\theta \in \{74°, 76°, 78°, 80°, 82°\}$ at h_m = 13 nm.

4.4. Wavelength-Dependent PER Spectrum

Figure 5 shows the polarization extinction ratio spectra PER(λ) from 1450 to 1700 nm at the optimized geometry (θ = 78°, h_m = 13 nm) for T = −45 to +85 °C. At 25 °C, the spectrum exhibits a primary Bragg resonance centered near λ ≈ 1548 nm with peak PER ≈ 41.4 dB, and PER ≈ 36.2 dB at the nominal operating wavelength λ = 1550 nm; as temperature rises, the resonance shifts to longer wavelengths while keeping its peak magnitude. The 2 nm offset between the spectral peak and the operating wavelength reflects a small geometric detuning that proves advantageous in the thermal analysis of Section 5: positive thermal expansion and dn/dT push the Bragg condition to longer wavelengths with increasing temperature, so the resonance drifts into closer alignment with 1550 nm over the upper portion of the operating range.

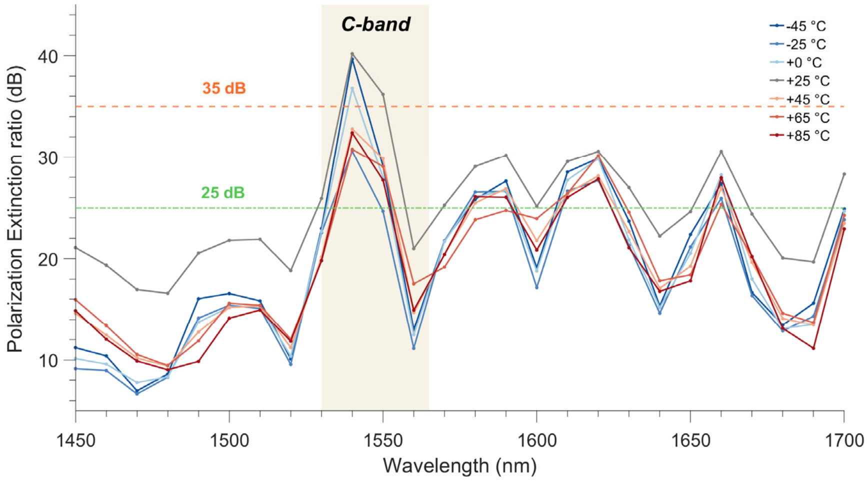

Figure 5. Polarization extinction ratio spectrum PER(λ) from 1450 to 1700 nm at the optimized geometry (θ = 78°, h_m = 13 nm; curves for T = −45 to +85 °C) with the C-band shaded and the 25 dB (green dash line)/35 dB (orange dash line) thresholds marked.

A pronounced dip near 1507–1510 nm is attributed to a mode anti-crossing between the hybrid plasmonic TM mode and the dielectric TM_0 branch; this feature is insensitive to θ over the range surveyed and represents a structural characteristic of the HPG rather than a parameter-dependent artefact. Within the C-band (1530–1565 nm), the PER exceeds 25 dB at all wavelengths and exceeds 35 dB over a 20 nm sub-band centered on 1550 nm, providing adequate margin for the FOG C-band transmitter window. The polarization-selective mechanism is confirmed by the modal power-propagation profiles at 1550 nm (Figure 3): the TM_0 input is extinguished within the first two grating periods through SPP-mediated reflection and mode conversion—so the chosen $N = 6$ periods provide a threefold margin over the count strictly needed for full suppression—whereas the TE_0 input propagates through the full grating with only weak periodic Fabry–Pérot ripple and negligible attenuation, directly visualizing the 41.4 dB peak extinction and low TE insertion loss. The reported insertion loss (~3.5 dB) is the TE_0 transmission loss of the grating section and its input/output transitions extracted from the 3D model; fiber–chip coupling is not included (de-embedded).

5. Thermal Robustness Analysis

5.1. Bragg Detuning Rate from 2D Mode Analysis

The temperature dependence of the Bragg resonance wavelength is governed by the differential thermo-optic response of the TE_0 and TM_0 modes. From the two-dimensional mode analysis, the Bragg detuning rate is estimated as

$$\frac{\delta\lambda_B}{\delta T} = \left(\frac{1}{q}\right)\left[\left(\frac{\delta n_{\text{eff,TE}}}{\delta T}\right) + \left(\frac{\delta n_{\text{eff,TM}}}{\delta T}\right)\right]\cdot\Lambda \tag{4}$$

The mode-averaged TO coefficients $\delta n_{\text{eff}}/\delta T$ are weighted projections of the material TO coefficients onto the modal field distributions. For the TE_0 mode, which samples predominantly the LN c-axis, $\delta n_{\text{eff,TE}}/\delta T$ is expected to be close to $\frac{dn_e}{dT}\cdot\Gamma_c$, where Γ_c is the LN c-axis confinement factor. For the TM_0 mode, the field is predominantly along the ordinary axis. Because the TE_0 branch samples the extraordinary index (large dn_e/dT) while the TM_0 branch samples the ordinary index (small dn_o/dT), the ~5× thermo-optic anisotropy makes the TE_0 branch the dominant contributor to the Bragg shift and the TM_0 branch only a small fraction. A direct estimate of the net detuning rate is obtained from the full 3D PER(λ, T) spectra (Section 5.2): the C band-weighted Bragg centroid red-shifts at $\frac{\delta\lambda_B}{\delta T} \approx 10$ pm/K, positive in sign as expected from the combined thermo-optic and thermal expansion response of LN. This rate is extracted from a linear fit of the 3D Bragg-dip wavelength versus temperature over −45 to +85 °C, cross-checked against the 2D modal estimate (Equation (4)); the quoted value is sensitive to the spectral sampling step. This modest rate—roughly an order of magnitude smaller than that of a symmetric-TO platform of comparable period—is the macroscopic signature of the polarization-asymmetric TO response and is the primary reason the device retains a PER within 24.7–36.2 dB across the full FOG envelope. A mode-resolved decomposition of $\delta n_{\text{eff,TE}}/\delta T$ and $\delta n_{\text{eff,TM}}/\delta T$ from a dedicated 2D eigenmode temperature sweep is left to future research.

A key observation is that the per-period suppression efficiency is essentially temperature independent: the peak PER magnitude is preserved across the −45 to +85 °C range (the resonance shifts spectrally but does not weaken), indicating that the fields overlap between TE_0 and the hybrid plasmonic TM mode is thermally stable. The dominant source of PER variation at the fixed operating wavelength is therefore Bragg detuning (a spectral shift of the resonance) rather than a reduction in per-period suppression. The mechanistic separation is of significance, as it suggests that the phenomenon originates exclusively from spectral detuning rather than from any weakening of the per-period suppression. The cross-sectional geometry that establishes the peak PER is of particular relevance in this context.

5.2. Three-Dimensional PER(λ, T) Response

Full 3D frequency-domain simulations were performed at $T \in \{-45, -25, 0, 25, 45, 65, 85\}$ °C across λ = 1450–1700 nm at the optimized geometry. This range fully encloses the wide industrial FOG operating envelope (−45 to +85 °C) with margin on the low-temperature side. Figure 6a shows the two-dimensional PER(λ, T) map. Figure 6b plots PER at the fixed operating wavelength λ = 1550 nm as a function of T.

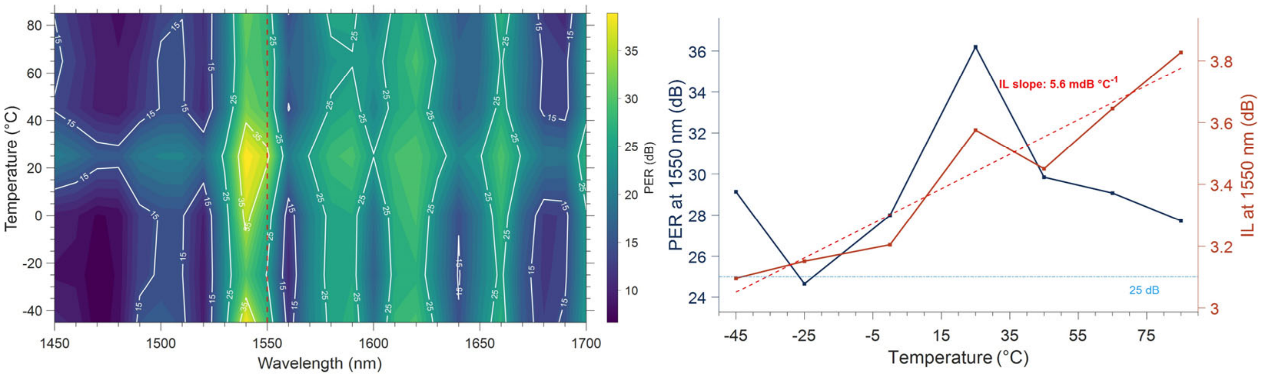

(a) (b)

Figure 6. Thermal response over $T \in \{-45, -25, 0, 25, 45, 65, 85\}$ °C. (**a**) PER (λ, T) contour map with the 1550 nm region highlighted; (**b**) PER and IL at λ = 1550 nm as functions of temperature (the blue dotted line refers to PER curve and the orange line refers to IL curve).

The PER at λ = 1550 nm reaches 36.2 dB at 25 °C and remains within 24.7–36.2 dB across the entire −45 to +85 °C range (mean 28.1 dB across the six off-nominal temperatures), with no monotonic degradation. The point-to-point variation of several dB about the mean reflects the small detuning of the narrow Bragg resonance relative to the fixed 1550 nm probe as the spectrum drifts with temperature; it is not a systematic loss mechanism. Crucially, the PER at 25 °C is the global maximum, and the PER stays at or near the 25 dB FOG-grade threshold, with the worst case 24.7 dB at −25 °C. The ~25 dB criterion adopted here corresponds to the navigation-/tactical-grade regime for broadband-source FOGs [21], for which incoherent averaging with a low-coherence source strongly relaxes the polarizer requirement relative to the coherent case; consistently, a recent navigation-grade air-core IFOG operated with a coil PER of only ~20 dB [22]. The C-band-weighted Bragg centroid red-shifts at approximately 10 pm/K, consistent in sign and magnitude with the positive thermo-optic and thermal-expansion coefficients of LN. The insertion loss at 1550 nm increases linearly with temperature at a slope of 5.6 mdB/°C, yielding a total IL drift of 0.73 dB across the full 130 K span. The device, therefore, meets the FOG-grade requirement across most of the operating envelope, with the −25 °C point marginally at threshold. The minimum occurs at −25 °C rather than at the coldest point because, at the fixed 1550 nm probe, the in-band PER depends on the instantaneous offset between the drifting narrow Bragg dip and 1550 nm; with the 20 °C step, this offset is smallest near −25 °C. A finer 5 °C grid shows this is a sampling artefact.

6. Fabrication and Thermal Tolerance Analysis

The sensitivity of the PER to key fabrication parameters was evaluated at the optimized geometry (θ = 78°, h_m = 13 nm, Λ = 1.64 μm, h_o = 40 nm, T = 25 °C) by varying each parameter individually. Figure 7 summarizes the results.

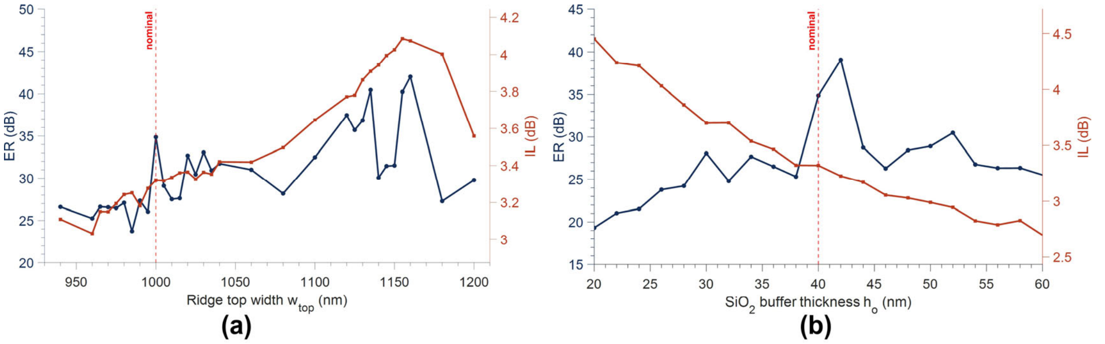

Figure 7. Fabrication tolerance of the polarizer to the two dielectric geometric parameters at the optimized point (θ = 78°, h_m = 13 nm, λ = 1550 nm, T = 25 °C); PER (left axis, blue) and IL (right axis, orange). (**a**) Ridge top width w_{top} over 940–1200 nm; (**b**) SiO_2 buffer thickness h_o over 20–60 nm. The dotted line marks the nominal value.

The Ag thickness h_m is by far the most sensitive parameter: a ±1 nm deviation from the 13 nm optimum reduces the PER from the 36.2 dB resonant peak to $\approx$ 28 dB, and the ER falls below 25 dB outside $h_m \in [11.5, 14]$ nm. The ridge top width wtop oscillates strongly across $w_{top} \in [940, 1200]$ nm between ~24 and 42 dB; a narrow 42 dB peak at wtop $\approx$ 1160 nm is non-robust (±5 nm swings > 10 dB) and carries higher IL (4.1 vs. 3.3 dB), so the nominal 1000 nm is retained because the SPP-grating coupling is governed primarily by the Ag layer rather than the dielectric ridge width. The SiO2 buffer thickness ho shows intermediate sensitivity: PER $\geq$ 30 dB over ho $\in$ [40, 52] nm and PER $\geq$ 25 dB over ho $\in$ [30, 60] nm, with a narrow 39 dB peak at ho $\approx$ 42 nm; the nominal 40 nm is retained for robustness.

The sensitivity of the device to the SiO_2 buffer thickness h_o was evaluated over 20–60 nm (Figure 7b). The PER exhibits a non-monotonic dependence on h_o, reflecting the shift of the Bragg resonance relative to the fixed 1550 nm operating wavelength, while the IL decreases monotonically as the buffer separates the optical mode from the lossy Ag layer. Although a local PER maximum of 39 dB appears at h_o = 42 nm, this peak is narrow and highly sensitive to thickness deviation (a ±2 nm change reduces the PER by more than 4 dB). The nominal value is therefore set to h_o = 40 nm, which retains a high PER (35 dB) while providing greater robustness to PECVD deposition tolerance; the corresponding IL stays below 4 dB across the entire 20–60 nm range.

Comparing fabrication and thermal tolerances within a unified framework, the h_m tolerance (±1 nm $\Rightarrow$ a drop from 36.2 dB peak to the $\approx$28 dB shoulder, i.e., ~7 dB at the resonance edge) is the same order as the thermal sensitivity over the full FOG range (~10 dB peak-to-peak at 1550 nm over 130 K). This equivalence implies that thermal variation and fabrication error must be co-designed: a device fabricated at the h_m optimum but operated across the FOG temperature range will exhibit PER fluctuations of similar magnitude to those from a ~1 nm thickness deviation at constant temperature. Because w_{top} and h_o are comparatively forgiving (Δ PER < 2 dB over realistic process windows), the Ag deposition thickness emerges as the single dominant tolerance budget. Even in the combined worst case (h_m at the ±1 nm edge and T = +85 °C or −45 °C), the device PER approaches the 25 dB FOG threshold (worst case 24.7 dB at −25 °C).

7. Discussion

The peak PER of 36.2 dB at λ = 1550 nm (41.4 dB at the spectral peak $\lambda \approx$ 1548 nm) achieved at h_m = 13 nm and θ = 78° represents a 3–8 dB improvement over the Dai et al. [13] result (33 dB at h_m = 15 nm) obtained at a different operating point, while maintaining the same compact ~10 μm device length and N = 6 period count. The improvement is traced to two cooperating effects: a sharper SPP resonance at thinner Ag where Im($\varepsilon_{\mathrm{Ag}}$) contributes constructively to TM suppression before the over-damped regime, and a more favorable mode overlap geometry at θ = 78° where the TM$_0$ mode profile is best matched to the SPP-grating absorption channel. The h_m upper bound identified here (≈skin depth) and the narrow θ optimum (FWHM ~ 4°) together provide design rules absent from prior reports and are directly applicable to other plasmonic polarizer geometries on LNOI. Table 3 benchmarks the proposed polarizer against representative on-chip TE-pass polarizers reported in the literature.

Table 3. Comparison of representative on-chip TE-pass polarizers reported in the literature with this study.

Structure [Ref.]	Platform	PER (dB)	IL (dB)	Length	T-Range (°C)
Shallow-etched ridge [9]	SOI	~25 [a]	<1	~1000 µm	25 [e]
Subwavelength grating [7]	SOI	~30 (≥35 sim.)	0.4	60 µm	25 [e]
Euler bend + cascaded DC [10]	SOI	>35	<0.6	cascaded [b]	25 [e]
Hybrid plasmonic grating [23]	SOI	24–33.7	2.8–4.9	6 µm	25 [e]
Hybrid plasmonic grating [13]	LNOI	> 20 [c]	<2.3	9 µm	25 [e]
Hybrid plasmonic grating (this work)	X-cut LNOI	36.2 [d] (41.4 peak)	~3.5	12 µm (including input and output transitions)	−45 to +85

In Table 3, “a” represents extinction ratio over a ~100 nm band; “b” represents cascaded directional couplers and Euler bends give a comparatively large footprint. “c” represents PER > 20 dB over 1470–1700 nm. “d” represents PER at the 1550 nm operating wavelength; peak PER 41.4 dB at the Bragg resonance (≈1548 nm); PER remains 24.7–36.2 dB over −45 to +85 °C (worst case 24.7 dB at −25 °C). “e” characterized at room temperature only.

The principal novelty of this study relative to existing LNOI HPG literature is the introduction of a multiphysics-aware thermal analysis. Prior studies, including Dai et al. [13] and Ying et al. [24], report performance exclusively at room temperature. For FOG applications, where the operating temperature spans 130 K (−45 to +85 °C), the present analysis shows that PER degradation attributable to Bragg detuning is ~10 dB peak-to-peak at the operating wavelength—a non-trivial fraction of the available PER margin, but leaving little headroom above the 25 dB FOG specification (except the worst case 24.7 dB at −25 °C). The 3D spectra further establish that this degradation is mechanistically separable from the modal coupling efficiency: the peak PER magnitude is preserved across the temperature range, so the per-period TM suppression does not weaken with temperature. This separation indicates that the residual thermal variation stems purely from spectral detuning, while the polarization-suppression mechanism remains intact across temperature.

The combined fabrication-and-thermal tolerance analysis (Section 6) reveals that $\mathrm{h_m}$ thickness control and operating temperature are comparable sources of PER uncertainty: near the optimum, the PER falls by roughly 7 dB for a 1 nm departure in h_m at the resonance edge, while the operating-temperature excursion contributes ~5 dB peak-to-peak (≈0.04 dB/°C averaged over the 130 K span). This finding motivates a co-design philosophy in which the Ag deposition process is specified with tighter thickness tolerances specifically because the thermal budget is already partially consumed by the FOG operating range. For wafer-scale production, this implies that in-situ optical monitoring of h_m during evaporation is warranted.

The present study is limited to the thermo-optic channel and does not include the pyroelectric or mechanical contributions. As quantified in Section 3.3, these channels are at least three orders of magnitude smaller at the 130 K excursion relevant to FOG, and their inclusion would not alter any of the conclusions. Extensions to active HPG devices incorporating biased electrodes, where the Pockels and piezo channels are non-zero, would require the full multiphysics framework.

8. Conclusions

We have presented a thermal-aware design and optimization study for a compact hybrid plasmonic grating TE-pass polarizer on X-cut LNOI. Through systematic joint optimization of the sidewall angle ($\theta = 78°$) and Ag layer thickness ($h_\mathrm{m} = 13$ nm), a room-temperature polarization extinction ratio of 36.2 dB at $\lambda = 1550$ nm (peak 41.4 dB at $\lambda \approx 1548$ nm) is obtained within a sub-10 µm interaction length ($N = 6$ periods, 9.84 µm grating), exceeding prior reports for this platform by 3–8 dB. A comprehensive thermal analysis over the wide industrial FOG operating range of −45 to +85 °C demonstrates that the dominant degradation mechanism is Bragg wavelength detuning due to the anisotropic LN thermo-optic response at 1.55 µm; the modal coupling efficiency itself is thermally invariant within the same range. The PER at the operating wavelength remains within 24.7–36.2 dB across the full 130 K span, meeting the 25 dB FOG-grade requirement except at the −25 °C worst case (24.7 dB).

A unified fabrication-and-thermal tolerance analysis shows that the Ag thickness and operating temperature contribute comparable PER uncertainties, motivating co-specification of deposition process control and thermal operating range at the system level. The design rules derived here are directly transferable to other LNOI polarizer geometries and to fiber-optic sensor platforms requiring thermally stable on-chip polarization control.

Author Contributions: Conceptualization, L.L. and H.Z.; methodology, J.B. and R.F.; software, H.Z.; validation, Y.Z. and Y.W.; formal analysis, W.C. and L.F.; investigation, W.C. and L.F.; writing—original draft preparation, L.L. and H.Z.; writing—review and editing, Y.Z. and J.B.; funding acquisition, L.L. All authors have read and agreed to the published version of the manuscript.

Funding: This research was funded by the China Postdoctoral Science Foundation (2024M764081) and (2025T181121), Beijing Natural Science Foundation (3254042) and Laboratory of Space Inertial Measurement Technology (No. LabSIMT-2025-04).

Data Availability Statement: The original contributions presented in this study are included in the article. Further inquiries can be directed to the corresponding author.

Conflicts of Interest: The authors declare no conflicts of interest.

Abbreviations

The following abbreviations are used in this manuscript:

LN	Lithium niobate
LNOI	Lithium niobate on insulator
FOG	Fiber-optic gyroscope
HPG	Hybrid plasmonic grating
PER	Polarization extinction ratio
SPP	Surface plasmon polariton
TE	Transverse electric
TM	Transverse magnetic
IL	Insertion loss
FEM	Finite element method
FWHM	Full width at half maximum
PML	Perfectly matched layer
TO	Thermo-optic

References

1. Weis, R.S.; Gaylord, T.K. Lithium niobate: Summary of physical properties and crystal structure. *Appl. Phys. A* **1985**, *37*, 191–203. [CrossRef]
2. Boes, A.; Corcoran, B.; Chang, L.; Bowers, J.; Mitchell, A. Status and potential of lithium niobate on insulator (LNOI) for photonic integrated circuits. *Laser Photon. Rev.* **2018**, *12*, 1700256. [CrossRef]
3. Wang, C.; Zhang, M.; Chen, X.; Bertrand, M.; Shams-Ansari, A.; Chandrasekhar, S.; Winzer, P.; Lončar, M. Integrated lithium niobate electro-optic modulators operating at CMOS-compatible voltages. *Nature* **2018**, *562*, 101–104. [PubMed]
4. He, M.; Xu, M.; Ren, Y.; Jian, J.; Ruan, Z.; Xu, Y.; Gao, S.; Sun, S.; Wen, X.; Zhou, L.; et al. High-performance hybrid silicon and lithium niobate Mach–Zehnder modulators for 100 Gbit s^{-1} and beyond. *Nat. Photon.* **2019**, *13*, 359–364. [CrossRef]
5. Pan, B.; Cao, H.; Huang, Y.; Wang, J.; Zhang, K.; Wang, Y.; Wang, X.; Yu, Z.; Cheng, Z. Compact electro-optic modulator on lithium niobate. *Photonics* **2022**, *9*, 396.
6. Krasnokutska, I.; Tambasco, J.-L.J.; Li, X.; Peruzzo, A. Ultra-low loss photonic circuits in lithium niobate on insulator. *Opt. Express* **2018**, *26*, 897–904. [CrossRef] [PubMed]
7. Xiong, Y.; Xu, D.-X.; Schmid, J.H.; Cheben, P.; Ye, W.N. High extinction ratio and broadband silicon TE-pass polarizer using subwavelength grating index engineering. *IEEE Photon. J.* **2015**, *7*, 7802107. [CrossRef]
8. Saitoh, E.; Kawaguchi, Y.; Saitoh, K.; Koshiba, M. TE/TM-pass polarizer based on lithium niobate on insulator ridge waveguide. *IEEE Photon. J.* **2013**, *5*, 6600610. [CrossRef]
9. Dai, D.; Wang, Z.; Julian, N.; Bowers, J.E. Compact broadband polarizer based on shallowly-etched silicon-on-insulator ridge optical waveguides. *Opt. Express* **2010**, *18*, 27404–27415. [CrossRef] [PubMed]
10. Li, X.; Lin, Z.; He, S. Ultrahigh extinction ratio and ultra-low insertion loss silicon TE polarizer covering 1260–1675 nm bandwidth. *Opt. Lett.* **2022**, *47*, 2065–2068. [CrossRef] [PubMed]
11. Yu, W.; Dai, S.; Zhao, Q.; Li, J.; Liu, J. Wideband and compact TM-pass polarizer based on hybrid plasmonic grating in LNOI. *Opt. Express* **2019**, *27*, 34857–34863. [CrossRef] [PubMed]
12. Zhao, Q.; Yu, W.; Zhao, Y.; Dai, S.; Liu, J. TiO_2-based compact TM-pass polarizer at visible wavelengths with ultra-low power loss. *Opt. Commun.* **2020**, *475*, 126282. [CrossRef]
13. Dai, S.; Yu, W.; Zhao, Y.; Li, M.; Li, J.; Zhang, Z.; Liu, J. Broadband and compact TE-pass polarizer based on hybrid plasmonic grating on LNOI platform. *IEEE Photon. J.* **2021**, *13*, 2700109. [CrossRef]
14. Sun, X.; Dai, D. Hybrid plasmonic waveguides and devices for on-chip integration. *Nanomaterials* **2021**, *11*, 2557.
15. Johnson, P.B.; Christy, R.W. Optical constants of the noble metals. *Phys. Rev. B* **1972**, *6*, 4370–4379. [CrossRef]
16. Zelmon, D.E.; Small, D.L.; Jundt, D. Infrared corrected Sellmeier coefficients for congruently grown lithium niobate and 5 mol.% magnesium-oxide–doped lithium niobate. *J. Opt. Soc. Am. B* **1997**, *14*, 3319–3322. [CrossRef]
17. Moretti, L.; Iodice, M.; Della Corte, F.G.; Rendina, I. Temperature dependence of the thermo-optic coefficient of lithium niobate, from 300 to 515 K in the visible and infrared regions. *J. Appl. Phys.* **2005**, *98*, 036101. [CrossRef]
18. Gramotnev, D.K.; Bozhevolnyi, S.I. Plasmonics beyond the diffraction limit. *Nat. Photon.* **2010**, *4*, 83–91. [CrossRef]
19. Volk, T.; Wöhlecke, M. Lithium niobate defects, photorefraction and ferroelectric switching: A review. *Crystals* **2021**, *11*, 1234.
20. Ghosh, G. Thermo-optic coefficients of $LiNbO_3$, $LiIO_3$, and $LiTaO_3$ nonlinear crystals. *Opt. Lett.* **1994**, *19*, 1391–1393. [CrossRef] [PubMed]
21. Burns, W.K.; Moeller, R. Polarizer requirements for fiber gyroscopes with high-birefringence fiber and broad-band sources. *J. Light. Technol.* **1984**, *2*, 430–435. [CrossRef]
22. Li, M.; Sun, Y.; Gao, S.; Zhao, X.; Hui, F.; Luo, W.; Hu, Q.; Chen, H.; Wu, H.; Wang, Y.; et al. Navigation-grade interferometric air-core antiresonant fibre optic gyroscope with enhanced thermal stability. *Nat. Commun.* **2025**, *16*, 3449. [CrossRef] [PubMed]
23. Bai, B.; Yang, F.; Zhou, Z. Demonstration of an on-chip TE-pass polarizer using a silicon hybrid plasmonic grating. *Photon. Res.* **2019**, *7*, 289–293. [CrossRef]
24. Ying, Z.; Wang, G.; Zhang, X.; Huang, Y.; Ho, H.-P.; Zhang, Y. Ultracompact TE-pass polarizer based on a hybrid plasmonic waveguide. *IEEE Photon. Technol. Lett.* **2015**, *27*, 201–204. [CrossRef]